Spatially Controlled Single Photon Emitters in hBN-Capped WS$_2$ Domes

Salvatore Cianci, Elena Blundo, Federico Tuzi, Giorgio Pettinari,
Katarzyna Olkowska-Pucko, Eirini Parmenopoulou, Djero B. L. Peeters,
Antonio Miriametro, Takashi Taniguchi, Kenji Watanabe, Adam Babinski,
Maciej R. Molas, Marco Felici,* and Antonio Polimeni*

Monolayers (MLs) of transition-metal dichalcogenides host efficient single-photon emitters (SPEs) usually associated to the presence of nanoscale mechanical deformations or strain. Large-scale spatial control of strain would enhance the scalability of such SPEs and allow for their incorporation into photonic structures. Here, the formation of regular arrays of *strained* hydrogen-filled one-layer-thick micro-domes obtained by H-ion irradiation and lithography-based approaches is reported. Typically, the H$_2$ liquefaction for temperatures $T<32$ K causes the disappearance of the domes preventing their use as potential SPEs. Here, it is shown that the dome deflation can be overcome by hBN heterostructuring, that is by depositing thin hBN flakes on the domes. This leads to the preservation of the dome structure at all temperatures, as found by micro-Raman and micro-photoluminescence (μ-PL) studies. Eventually, spatially controlled hBN-capped WS$_2$ domes show the appearance, at 5 K, of intense emission lines originating from localized excitons, which are shown to behave as quantum emitters here. The electronic properties of the emitters are addressed by time-resolved μ-PL yielding time decays of 1–10 ns, and by magneto-μ-PL measurements. The latter provide an exciton magnetic moment a factor of two larger than the value observed in planar strain-free MLs.

1. Introduction

Transition metal dichalcogenides (TMDCs) in the monolayer (ML) form have been extensively studied since the discovery of the direct nature of their bandgap,[1–5] making them ideal candidates for flexible opto-electronic devices.[6–8] Indeed, the 2D nature of these materials and their exceptional robustness to mechanical deformations[9–16] have opened an entire field of research dedicated to the study of the effects of lattice deformations (strain) on the material electronic and optical properties.[17]

Strain gradients in TMDC MLs have also been related to the appearance of single-photon emitters (SPEs) at cryogenic temperatures,[18–26] greatly increasing the potential of these materials for quantum technologies. Indeed, layered materials are advantageous from a production point of view—since bulk crystals provide many exfoliable MLs—and by virtue of the high extraction efficiency of the emitted photons,

S. Cianci, E. Blundo, F. Tuzi, E. Parmenopoulou, D. B. L. Peeters,
A. Miriametro, M. Felici, A. Polimeni
Physics Department
Sapienza University of Rome
Rome 00185, Italy
E-mail: marco.felici@uniroma1.it; antonio.polimeni@uniroma1.it
G. Pettinari
Institute for Photonics and Nanotechnologies (CNR-IFN)
National Research Council
Rome 00133, Italy

K. Olkowska-Pucko, A. Babinski, M. R. Molas
Institute of Experimental Physics
Faculty of Physics
University of Warsaw
Warsaw 02-093, Poland

D. B. L. Peeters
Department of Applied Physics and Science Education
Eindhoven University of Technology
Eindhoven 5600 MB, The Netherlands

T. Taniguchi
International Center for Materials Nanoarchitectonics
National Institute for Materials Science
1-1 Namiki, Tsukuba 305-0044, Japan

K. Watanabe
Research Center for Functional Materials
National Institute for Materials Science
1-1 Namiki, Tsukuba 305-0044, Japan

**ADVANCED
SCIENCE NEWS**

www.advancedsciencenews.com

**ADVANCED
OPTICAL
MATERIALS**

www.advopticalmat.de

due to the lack of internal reflection. Even though the link between strain gradients and SPEs in TMDCs is yet to be fully understood, in the last few years several different structures (e.g., etched holes,[19] nanorods,[27,28] nanopillars,[29–31] nanowires,[32] nanostars,[33] etc.) have been used as stressors for TMDC MLs to generate ordered arrays of SPEs. Moreover, by exploiting plasmonic effects[28,31,33,34] and optical cavities[35,36] in which these 2D systems can be easily integrated, it is possible to enhance the emitter brightness by increasing their radiative recombination rate.

In order to advance the field of quantum nanotechnologies, single-photon sources should be produced using manufacturing methods that are cheap, scalable, reproducible, and preferably compatible with current photonic integration technologies. In particular, among the numerous ways by which a strained TMDC ML can be obtained, for example, deposition on dissimilar substrates, bending, bulging, or indenting devices etc.,[17] low-energy hydrogen irradiation of bulk flakes has been proven to be a reliable and efficient way to form strained, ML-thick, H_2-filled bubbles, hereafter called *domes*, on the surface of the irradiated flakes.[37] These domes feature radii ranging from tens of nm to a few µm and their size and position can be controlled by the lithographic definition of H-opaque masks on the flake surface, prior to the irradiation process, leading to the formation of µm- (or even nm-) sized light emitters at room temperature (RT).[37] However, when brought to cryogenic temperatures, the domes deflate due to the gas-to-liquid transition of molecular hydrogen, taking place at a critical temperature $T_C \approx 32$ K (the domes then reversibly re-inflate if the temperature is increased above T_C).[37] Here, we show how to prevent the deflation of the domes via deposition (capping) of few-layer-thick hexagonal boron nitride (hBN) on top of the domes. The striking preservation of the dome shape, and corresponding strain field, via hBN capping is investigated by means of µ-Raman spectroscopy performed on MoS_2 domes and of micro-photoluminescence (µ-PL) spectroscopy performed on an ordered array of WS_2 domes. Importantly, this phenomenon is here exploited to create site-controlled SPEs, which appear at low temperature (≈5 K) in the spectra of the hBN-capped WS_2 domes. The single-photon purity of these emitters was assessed by second-order auto-correlation measurements, and the SPE electronic properties were further investigated by time-resolved µ-PL and magneto-µ-PL measurements. These latter showed an exciton gyromagnetic factor much larger than that observed in strain-free WS_2 MLs providing an enhanced response of the exciton to external magnetic fields.

2. Results and Discussion

In this work, we will focus on MoS_2 and WS_2 crystals, even though the dome formation was also demonstrated for several other TMDC materials[37] and for hBN.[38] Such a choice is motivated by the experimental probes used to determine the dome strain, that is the particularly clear and intense Raman signal of MoS_2 and the high PL efficiency of WS_2.

WS_2 emitters were observed in regular arrays of domes obtained by hydrogenating a WS_2 bulk flake patterned with a lithographically-designed poly(methyl methacrylate) (PMMA) mask, whose openings (diameter, 3 µm) allow the space-

controlled formation of hydrogen-filled domes. We point out that PMMA self-cleans during the H-ion irradiation process, thus leaving the so-formed domes isolated and free from neighboring smaller domes or debris, a process that facilitates the subsequent deposition of hBN. The patterned hydrogen irradiation procedure was described in previous works[13,14,37] and more details are provided in the Experimental Section. **Figure 1**a shows an atomic force microscope (AFM) image of an ordered array of WS_2 domes capped with few-layer-thick (≈10 nm) hBN on a specific region marked by a white dashed line. The AFM image shows an optimal adherence of the hBN flake to the domes underneath, as well as the dome robustness against the capping process. The structural effects of the capping of the TMDC domes can be readily appreciated by looking at the optical microscope images of the sample at RT and 5 K shown in Figure 1b,c, respectively. The latter clearly shows the dome deflation in the uncapped region on the right top corner of the image, while the domes covered with hBN unexpectedly retain their shape with minimal differences in size.

In order to attain clues on this phenomenon and information on the variations of the dome strain with temperature, a bare MoS_2 dome (see AFM image in **Figure 2**a) was first studied by µ-Raman measurements at different T_s (see Experimental Section). The same study was then carried out after capping the dome with hBN (see AFM image in Figure 2b). The corresponding T-dependent µ-Raman spectra are shown in Figure 2c (bare) and Figure 2d (capped). The spectra referring to all temperatures can be found in Figure S1, Supporting Information. In both cases, the µ-Raman spectra were recorded on the center of the dome, where the tensile strain is maximum and features a biaxial character.[14,38,39] The µ-Raman spectra are characterized by the peaks associated to the in-plane (E_{2g}, Raman shift < 400 cm⁻¹) and out-of-plane (A_{1g}, Raman shift >400 cm⁻¹) normal modes of oscillation. Two contributions are present for each mode, one due to the bulk MoS_2 flake underneath the dome and the other associated to the ML-thick dome membrane. In the latter case, the Raman mode is found at lower frequency with respect to the bulk one, due to the inherent tensile strain of the domes.[39]

An immediately recognizable difference between the two sets of data regards the variation with T of the relative intensity of the dome and bulk peaks. Specifically, the signal from the bare MoS_2 dome exhibits a largely different intensity for different temperatures. This can be ascribed to the dome progressive deflation, which, in turn, affects the interference effect responsible for the amplification of the Raman signal occurring when the dome height matches about half the wavelength of the Raman signal (≈532/2 nm). Instead, the T-dependent spectra of the same dome after being capped with hBN exhibit a remarkable stability of the dome to bulk relative intensity even at the lowest temperature considered, offering evidence of the fact that the capped dome retains its shape, regardless of the hydrogen phase. Figure 2e displays the results of the Lorentzian fits performed on each µ-Raman spectrum, plotting the shift of the E_{2g} and A_{1g} peaks of the dome as a function of temperature. The Raman shift values were fitted with the formula

$$\omega(T) = \omega_0 + A\left[1 + 2/\left(e^{\frac{\hbar\omega_0}{2k_B T}} - 1\right)\right] \tag{1}$$

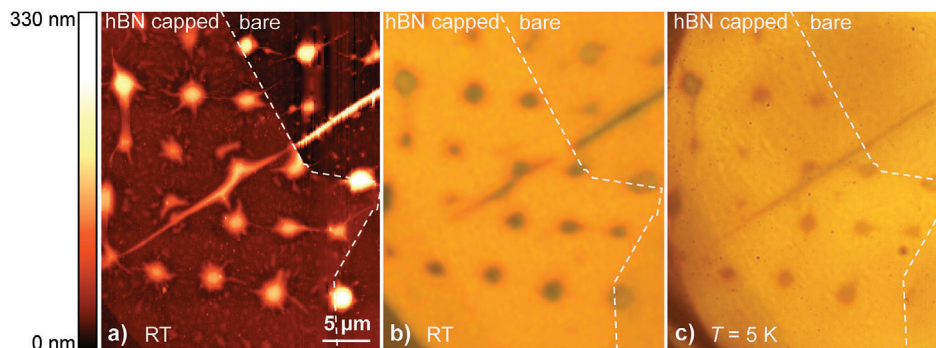**ADVANCED
SCIENCE NEWS**

www.advancedsciencenews.com

**ADVANCED
OPTICAL
MATERIALS**

www.advopticalmat.de

Figure 1. a) AFM image of an ordered array of WS_2 domes partially capped with a thin hBN flake (≈ 10 nm). The white dashed line marks the border between the uncapped or bare, area (top-right) and the remaining area capped with hBN. b) Optical microscope image of the same area of panel (a), taken at RT. c) Same as (b) but with the sample at 5 K. The domes in the capped area kept their shape, while those which were not capped with hBN clearly deflated. The lower quality of the image at $T = 5$ K is caused by the presence of the cryostat window.
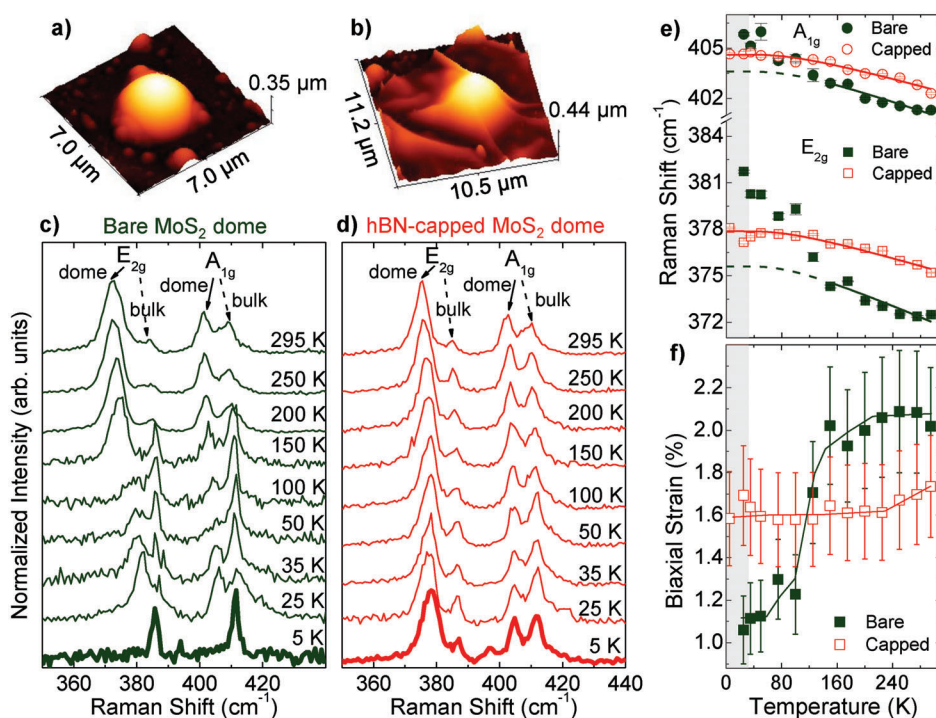

Figure 2. a) 3D AFM image of a bare MoS_2 dome. b) 3D AFM image of the same dome of panel (a) after the capping with hBN. Both images were taken at RT. c) Stacked normalized μ-Raman spectra at different temperatures of the bare MoS_2 dome. The peaks associated to the E_{2g} (in-plane) and A_{1g} (out-of-plane) modes of oscillation are visible for both the bulk material (indicated by a dashed arrow) and the dome membrane (indicated by a solid arrow). d) Stacked normalized μ-Raman spectra at different temperatures of the same MoS_2 dome of panel (c) after the capping with hBN. A laser excitation wavelength equal to 532 nm and laser power equal to 30 μW were employed for the spectra of panels (c,d). e) Temperature dependence of the E_{2g} (squares) and A_{1g} (circles) modes of the dome membrane before (olive, full) and after (red, empty) the hBN capping. The gray shaded area highlights the T interval for which hydrogen condenses (<32 K). The evolution in temperature is fitted (solid lines) via Equation (1). For the bare dome, the fit was performed for $T = 150 - 300$ K, where a well defined trend could be observed (the dashed lines are an extrapolation at lower temperatures). f) Values of the biaxial strain versus T for the bare (olive full squares) and capped (red empty squares) MoS_2 dome obtained from Equation (2). In the case of the capped dome the strain is kept constant even at the temperatures for which the hydrogen is no longer in the gas phase (gray shaded area). The lines are guides to the eye.

where only the lower-order three-phonon processes of the anharmonic Klemens model are taken into account via the parameter A.[40,41] The frequency trends of the dome peaks show a strong difference between the bare and capped configurations, with the latter featuring regular temperature shifts, even in the range of temperatures for which the hydrogen gas condenses (indicated in the plots by a shaded gray area). Instead, the bare dome is characterized by a much more erratic change in the frequency position of its Raman peaks, reflecting the major structural changes it undergoes at lower temperatures. For these reasons, only the peaks

**ADVANCED
SCIENCE NEWS**

www.advancedsciencenews.com

**ADVANCED
OPTICAL
MATERIALS**

www.advopticalmat.de

in the temperature range 150–300 K were fitted by Equation (1) with the resulting fit being indicated by an olive solid line. The line obtained from the fit is extended, for lower temperatures, by an olive dashed line, which highlights the stark contrast between the expected evolution in temperature and the actual measured frequencies. The Raman mode frequency of the reference unstrained ML, $\omega^{\mathrm{ML}}(T)$, can be obtained from the measured bulk mode by just adding (subtracting) a small (1.5 cm^{-1}), rigid shift to the E_{2g} (A_{1g}) peak.[39] Therefore, from the frequency position of the Raman peaks associated to the bulk and to the dome modes (the full set of data is shown in Supporting Figure S1, Supporting Information), the information on the biaxial strain ϵ at different temperatures can be extracted quantitatively by applying the following formula:

$$\epsilon(T) = \frac{1}{2} \times \left(\frac{\omega_{E_{2g}}^{\mathrm{ML}}(T) - \omega_{E_{2g}}^{\mathrm{dome}}(T)}{\omega_{E_{2g}}^{\mathrm{ML}}(T)} \right) \frac{1}{\gamma_{E_{2g}}} \quad (2)$$

where $\omega_{E_{2g}}^{\mathrm{ML}}(T)$ is the Raman shift of the in-plane mode of a strain-free MoS$_2$ ML at temperature T, $\gamma_{E_{2g}}$ is the Grüneisen parameter equal to 0.84 ± 0.11[39] (assumed constant at all temperatures[42]) and the total biaxial strain is divided by two to obtain the strain exerted on just one direction (i.e., the radial or the circumferential one that are equivalent at the top of the dome[39]). The strain values obtained with such a procedure are shown in Figure 2f. The evolution of the strain characterizing the bare dome (denoted by olive full squares) with decreasing T indicates that the dome membrane becomes progressively less stretched due to the diminishing pressure of the hydrogen gas inside. When the gas eventually condenses, for temperatures falling in the gray shaded area, the dome collapses onto the bulk crystal, so that the corresponding μ-Raman signal disappears at $T = 5$ K (see the bottom-most spectrum in Figure 2c). In the case of the capped MoS$_2$ dome, instead, the values of strain show virtually no evolution for all temperatures, as displayed by the red empty squares. The same strain evolution in temperature was observed for several other bare and capped MoS$_2$ domes, see Figure S2, Supporting Information. This provides further confirmation that MoS$_2$ domes can be rigidly and systematically kept in shape by the hBN layer deposited atop. Even though the exact mechanism by which the hBN thin flake causes such a phenomenon is still not understood, we envisage that the hBN high rigidity may play an important role. Additionally, it is noteworthy that at RT the capping procedure reduces the membrane strain from $\epsilon = 2\%$ to about 1.7% (see Figure 2f). This indicates a likely elastic energy transfer from the dome membrane to the capping hBN layer, which possibly provides the energy necessary to maintain the dome structure regardless of the inner hydrogen phase state. It is worth mentioning that hydrogen-filled strained domes made of hBN are also known to deflate at low T_s.[38,43] This proves the unique effect played by the capping process, during which the hBN flake adapts to the sample morphology to minimize the total energy of the system. In turn, the deflation of the dome underneath would imply a strain transfer to the hBN capping layer and thus an energy cost. The cost of keeping the dome in-shape is likely lower, leading to this peculiar effect. We also verified that the same structural effect is obtained by capping with hBN flakes hBN domes instead of TMDC domes.
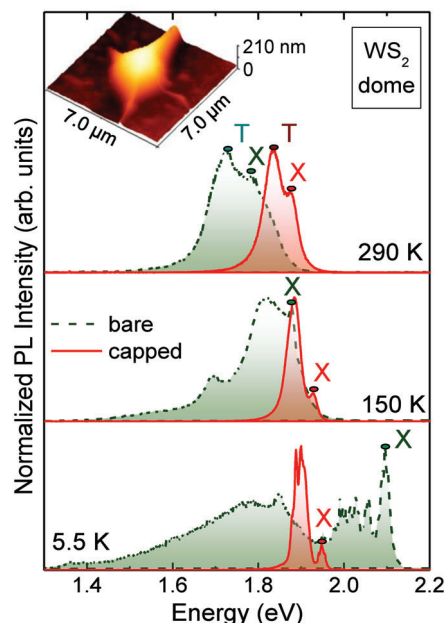

Figure 3. Stacked normalized μ-PL spectra taken at different temperatures on a WS$_2$ dome, before (olive dashed line) and after (red solid line) the capping with few-layer-thick hBN. Excitation wavelength equal to 532 nm and laser power equal to 44 μW. The free neutral exciton is indicated as X, while recombination from charged excitons (trions) is indicated with T. At $T = 290$ K, the X (and T) band of the capped dome is about 90 meV higher in energy than that of the bare dome indicating a sizable tensile strain reduction ensuing the capping. At lower temperatures, for the bare dome several bands contribute to the emission spectra likely originating from morphological defects associated to the progressively deflating membrane. On the contrary, the hBN-capped dome maintains a well-defined lineshape at all temperatures (the T band label is omitted for clarity purposes). The inset shows a 3D AFM map of the dome capped with hBN, taken at RT.

The effects of hBN capping were also investigated by performing μ-PL measurements (see Experimental Section) both prior to and after the capping procedure on the ordered array of WS$_2$ domes displayed in Figure 1. For these domes, we also performed Raman studies analogous to those performed on MoS$_2$ domes, see Figure S3, Supporting Information. Usually, the PL emission spectra of TMDC MLs are characterized by the presence of the band gap exciton peak,[44] whose recombination energy is highly sensitive to the amount of strain experienced by the ML.[17,45] For our system, the redshift of the exciton emission is intimately related to the evolution of the strain tensor across the dome surface.[37,46] In particular, the biaxial strain values that can be attained on top of the bare WS$_2$ domes are close to those necessary ($\epsilon \simeq 2.5\%$) to observe the direct-to-indirect band gap transition, as reported previously.[46,47]

Figure 3 illustrates the effects of hBN capping on the emission properties of a WS$_2$ dome belonging to the array shown in Figure 1. The spectra were recorded on the top of the dome both before (olive dashed lines) and after (red solid lines) the hBN capping. At 290 K, the first clear difference between the bare and capped configuration is a reduction in strain following the capping procedure, as demonstrated by the blueshift of the neutral exciton peak (labeled X) in the capped dome (the lower-energy

**ADVANCED
SCIENCE NEWS**

www.advancedsciencenews.com

**ADVANCED
OPTICAL
MATERIALS**

www.advopticalmat.de

bands, labeled T, can be attributed in both cases to charged exciton species[45,48]). This finding is in accordance with the μ-Raman results of the MoS$_2$ domes (see Figure 2 and related discussion). However, in the patterned WS$_2$ dome, the ≃90 meV blueshift of the exciton energy at 290 K indicates a remarkable biaxial strain reduction by about 1% after the hBN capping.[46] This points to an optimal adherence of the hBN layer over the dome surface thanks to the lithographic isolation of the patterned WS$_2$ domes that avoids the formation of satellite smaller domes around them (as demonstrated by the AFM images of an uncapped region of the sample shown in Figure S4, Supporting Information). This isolation does not occur in the randomly formed MoS$_2$ domes discussed previously (see AFM images in Figure 2a,b), where a smaller strain reduction was indeed found. When cooling the sample from RT, the changes in the bare dome morphology can be seen in the evolution of the dome emission spectrum, characterized by a broad lineshape with several contributing bands and by an exciton peak showing an anomalously large "thermal" blueshift of 250 meV. This value clearly contrasts the regular blueshift observed for the exciton of the capped dome (85 meV) when T decreases. Indeed, at 5.5 K the bare dome is completely deflated, and the peak visible at ≈2.1 eV comes from the WS$_2$ ML laying on the WS$_2$ bulk, being decoupled from this latter by the likely presence of condensed hydrogen. Lower-energy recombination bands ought to be ascribed to the morphologically disordered structure (e.g., wrinkles) of the deflated ML. As a matter of fact, the progressive decrease of tensile strain when the H$_2$ pressure inside the dome decreases induces a blueshift of the exciton energy that adds to the usual band gap increase with decreasing T. For decreasing T, the regular blueshift of the X peak of the capped dome (lower-energy bands are ascribable to charged exciton species) leads thus to a peculiar trend in which the capped dome exciton, compared to the bare one, is at higher energies for high temperatures and lower energies for low temperatures. A more detailed temperature study for this capped WS$_2$ dome can be found in the Figure S5, Supporting Information. In the same figure, it is also shown that the evolution in temperature of the X energy of the capped dome overlaps that of an unstrained WS$_2$ ML.

The hBN capping procedure—along with the high spatial control over the dome formation site—prompts the opportunity for the creation of light sources in TMDC materials. Indeed, one of the most striking features of the capping procedure is the appearance, in the μ-PL spectra of domes brought to low temperature, of intense, relatively narrow (full-width at half-maximum = 1–5 meV) and spectrally isolated lines, whose quantum nature will be shown next.

Previous studies already reported the appearance of SPEs in WSe$_2$ and WSSe MLs at low temperature. In many cases, their origin was ascribed to strain gradients, which are provided either by the wrinkling caused by the deposition procedure[25,49] or by nanostructured stressors, such as nanopillars, nanorods etc.[27,29,30,50] Even though the exact origin of these SPEs has not been fully clarified, yet, it is strongly suggested that they could stem from the interplay between dark states, strain gradients, and defect-related levels.[51–53] In particular, darkish materials such as WSe$_2$ and WS$_2$ are characterized by opposite spins in the bottom conduction band (CB) and in the top valence band (VB), resulting in a dark ground state. Indeed, strain lowers the CBs and, when it reaches a suitable value, may bring the lowest energy CB to become resonant with defect states, leading to a hybridization between the two.[51] While dark strain-localized exciton states remain dark, hybridization with a point defect breaks the valley selectivity and leads to efficient light emission.

In our system the strain gradient is naturally provided by the dome morphology with an ensuing strain increase from the edge to the top of the dome, where the strain is the largest.[37,39] Based on a theoretical ground, such a strain increases from the edge toward the summit should lead to the formation of localized states toward the dome apex, due to strain-induced quantum confinement.[54] However, in our system, by approaching the top of the dome, the exciton recombination character changes from direct to indirect, thus leading to a less intense emission.[46] As a matter of fact, we observe that the emitters appear almost exclusively at the edge of slightly asymmetric domes, as depicted in the optical images in the insets of **Figure** 4a,f. The images show the point of the domes excited by the laser spot from which the corresponding spectra displayed in the main panel originate. Our result is the first experimental investigation of micron-sized WS$_2$ domes, whose exciton character changes from direct to indirect from the edge toward the center. Some previous studies investigated instead TMDC nanodomes by near-field PL measurements at room temperature.[55] In that case, the presence of localized, deeply bound exciton states only in the dome periphery was reported.[55] Those nanodomes were created by deposition of a TMD ML on an hBN substrate (and ensuing encapsulation of contaminants), and the observation of SPEs at the dome periphery was explained in terms of atomic-scale wrinkling taking place at the edge of the nanodomes, thus causing strain maxima to be at the edges and not at the center, as theoretically supported by the findings of ref. [56]. The system simulated in that theoretical work also differs remarkably from ours, since it focuses on the study of a MoS$_2$ ML deposited over a MoS$_2$ ML. Indeed, the theoretical framework described in that work[56] and used to explain the near-field experiments[55] cannot be applied to our domes, which are created by a bottom-up approach (hydrogen-ion irradiation) resulting in well-clamped edges (with no wrinkling) and in a strain increase from the edges toward the center. We rather believe that the more pronounced direct character of the exciton at the edge of the domes along with the suitable strain extent act as the driving force leading to the appearance of the emitters therein.

The spectrum of Figure 4a features three distinct lines (labeled with the letters α, β, and γ), whose intensity for increasing laser power is shown in Figure 4b. For each line, the emission intensity displays the saturating behavior usually associated to discrete defect states[19] and described by the equation

$$I = I_{\text{sat}}\left[P/\left(P + P_{\text{N}}\right)\right] \tag{3}$$

where I_{sat} is the saturation intensity and P_{N} is the laser power at which the intensity is half of I_{sat}.

Time-resolved μ-PL measurements (see Experimental Section), performed by exciting the sample with a supercontinuum laser spectrally filtered at 532 nm, were taken for all these emitters in order to extract their decay time. In Figure 4c the PL decay curves of the emitters α, β, and γ are fitted with an exponential function, yielding time decay time values of (2.690 ± 0.029),
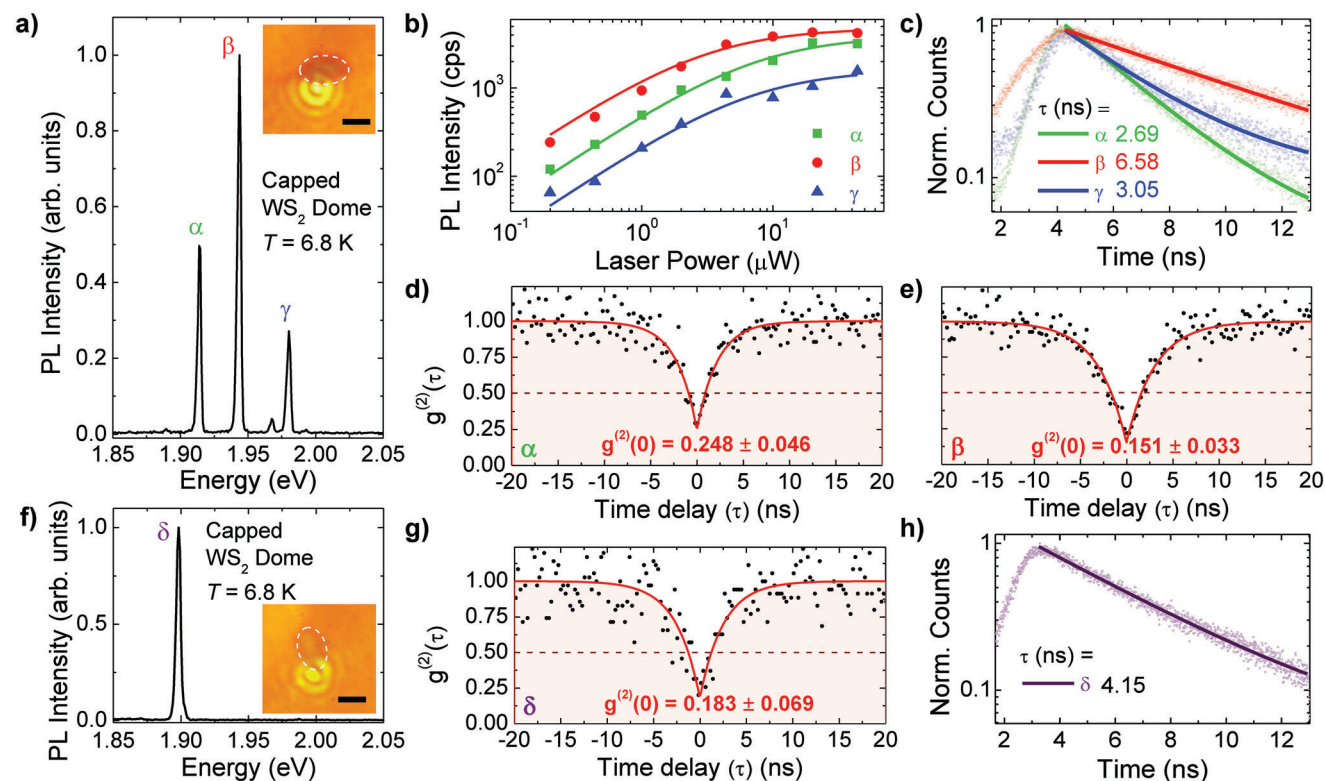
**ADVANCED
SCIENCE NEWS**

www.advancedsciencenews.com

**ADVANCED
OPTICAL
MATERIALS**

www.advopticalmat.de

Figure 4. a) Narrow lines (labeled α, β, and γ) in the μ-PL spectrum of a capped dome at 6.8 K. The excitation wavelength is 532 nm and the laser power is 200 nW. The right inset is an optical image, taken at 6.8 K, showing the dome's area excited by the laser. The white dashed line highlights the dome asymmetric profile. Scale bar 2 μm. b) Saturation of the PL intensity (*I*) for increasing laser power (*P*) of all the three lines featured in panel (a), fitted with Equation (3). c) Time-decay curves of the three emitters of panel (a) fitted with an exponential decay function. The decay times extracted from the fits are equal to (2.690 ± 0.029), (6.58 ± 0.20), and (3.045 ± 0.042) ns for the emitters α (green), β (red), and γ (blue), respectively. d,e) Second-order autocorrelation function $g^{(2)}(\tau)$ measured for emitter α (panel d) and β (panel e) whose values at zero-time delay are equal to 0.248 ± 0.046 and 0.151 ± 0.033. f) μ-PL spectrum of a different WS_2 dome capped with hBN at a temperature of 6.8 K. Laser power, 20 μW. The spectrally isolated emitter is labeled δ. The inset on the right shows an optical image of the dome and its area excited by the laser at 6.8 K. The white dashed line highlights the dome's asymmetric profile. Scalebar, 2 μm. g) Second-order autocorrelation function $g^{(2)}(\tau)$ measured for emitter δ, whose $g^{(2)}(0)$ value is equal to 0.183 ± 0.069. h) Time-decay curve of emitter δ fitted with an exponential decay function. The extracted decay time of (4.148 ± 0.055) ns.

(6.58 ± 0.20), and (3.045 ± 0.042) ns, respectively. All the obtained decay times are in accordance with those measured for localized states in WSe_2 MLs.[18–20,28–30,33,34,57] To determine whether the studied lines originate from quantum emitters, the second-order autocorrelation function $g^{(2)}(\tau)$ was measured for line α (Figure 4d) and β (Figure 4e). The samples were excited with a continuous-wave laser at 532 nm and the emission was filtered by a monochromator in order to select a specific emitter (see details on our Hanbury–Brown and Twiss setup in the Experimental Section). The autocorrelation function was not measured for line γ due to its lower intensity and to the presence of nearby smaller-intensity emissions that would have hindered the source purity. All the measured emitters display the characteristic antibunching dip at zero time delay, with values of $g^{(2)}(0)$ equal to 0.248 ± 0.046 and 0.151 ± 0.033 for the α and β emitters, respectively. The spectrum of another capped WS_2 dome is shown in Figure 4f, and it is characterized by the presence of a single, isolated emitter (labeled δ) that is observed by exciting the dome close to its edge. Figure 4g shows the second-order autocorrelation function of this line, whose behavior as an SPE is confirmed by a value of $g^{(2)}(0)$ equal to 0.183 ± 0.069. The corresponding

time-resolved μ-PL measurement is displayed in Figure 4h, and it shows a mono-exponential decay curve, whose fitting returns a decay time of (4.148 ± 0.055) ns. We point out that while most of the research interest on TMDC-based SPEs has been focused on WSe_2, WS_2 has been the object of much fewer studies.[24,29,58] Our work presents, to our knowledge, the first non-electrical generation of WS_2 SPEs, with the highest purity to date and the first measurement of the emitter decay time. We exclude that these emitters may come from the hBN capping layer since, i) emitters in hBN are typically created via electron irradiation, plasma treatments, and/or high-*T* annealings;[36,59,60] ii) emitters in hBN are typically broader, are distributed over a larger energy range and persist up to RT (unlike ours);[59,60] iii) we do not observe SPEs in the capped regions around the WS_2 domes, nor in hBN-capped MoS_2 domes, nor in hBN domes.

SPEs in TMDC MLs can be also relevant for valley- and spintronics applications. To this regard, the exciton gyromagnetic factor, *g*, is an important parameter determining the response of the carrier states to magnetic fields. It also represents an insightful quantity for understanding the properties of the band structure levels involved in the exciton recombination. Therefore, the emit-
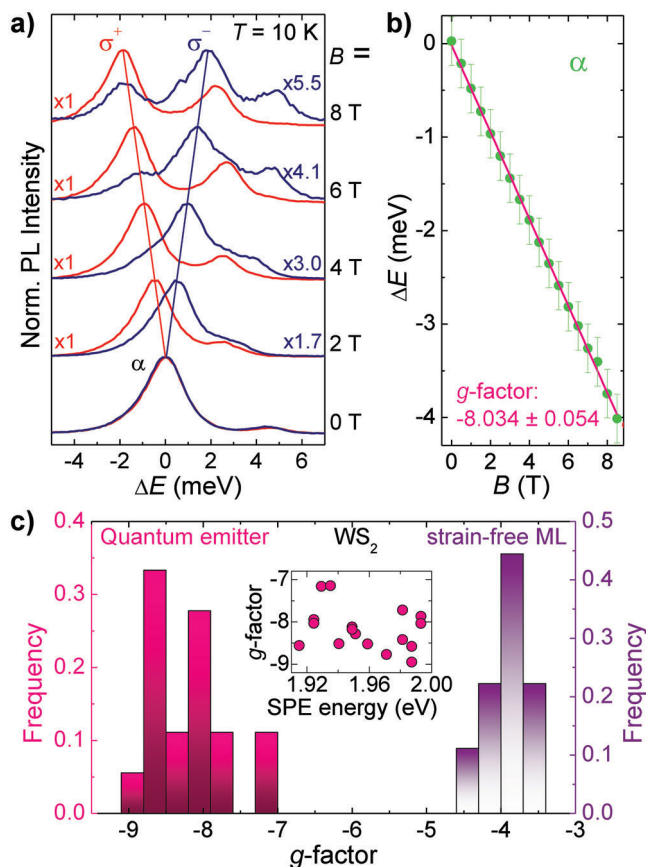
ADVANCED
SCIENCE NEWS

www.advancedsciencenews.com

ADVANCED
OPTICAL
MATERIALS

www.advopticalmat.de

Figure 5. a) Helicity-resolved normalized μ-magneto-PL spectra of the SPE labeled α in Figure 4a. In order to compensate for slight changes in the emission energy caused by a drift of the sample during the field sweep, the spectra are shifted on the x-axis with respect to the mean value in energy of the two polarizations. A splitting of a less intense line is also visible at higher energy. b) Zeeman splitting ΔE of the line of panel (a) as a function of the magnetic field. The linear fit, following Equation (4), gives a value of the exciton g-factor equal to -8.034 ± 0.054. c) In pink, we show the histogram the g-factors obtained by performing fits analogous to that of panel (b) on 18 narrow lines (see Figure S6, Supporting Information). The histogram is characterized by a mean value of $g = -8.20 \pm 0.51$. In purple, we show the histogram of the g-factors of the free exciton of unstrained WS$_2$ MLs. The histogram was built from the values available in the literature[47,62–69] giving a mean value of $g = -4.00 \pm 0.28$. The inset shows the correspondence between the energy of the SPE and their g-factor, showing no apparent correlation.

ters discussed above, as well as several others, were studied in the presence of a magnetic field (B) parallel to the luminescence wavevector (Faraday configuration) up to 12 T, at a temperature of 10 K (see Experimental Section). After being excited by a 515 nm laser, the light emitted from the sample is analyzed in terms of σ^+ and σ^- polarizations. **Figure 5**a shows the magneto-μ-PL spectra of line α displayed in Figure 4a. The intensity factors next to each spectrum show the increasing degree of circular polarization of the emission with increasing B, reaching a value of 69% at 8 T, which is consistent with the one obtained for similar emitters in WSe$_2$.[61] By fitting the spectra of the two circular polarizations with a Lorentzian function we can extract the Zeeman splitting

energy of the exciton $\Delta E(B) = E(\sigma^+) - E(\sigma^-)$, and from the relation

$$\Delta E = g\mu_{\rm B} B \tag{4}$$

(where $\mu_{\rm B}$ is the Bohr magneton) we can obtain the value of the exciton g-factor (Figure 5b). Emitters α and β (for this latter, refer to Figure S6(l), Supporting Information) have values of g equal to -8.034 ± 0.054 and -8.176 ± 0.025, respectively. The values of g related to several other narrow lines (see linear fits on the Zeeman splittings in Figure S6, Supporting Information) were collected in the pink histogram of Figure 5c, giving a mean value of $g = -8.20 \pm 0.51$. The additional high-energy peak visible in the spectra of Figure 5a was not included in this histogram since it is the only outlier of the distribution, with a g equal to -5.39 ± 0.13. This anomalous value of g requires further studies, since it could be linked to an excitonic species different from that of the other emitters.

Due to the lack of preceding results on the exciton g-factor of WS$_2$ SPEs, we compare our results with those of free excitons in strain-free WS$_2$ MLs reported in the literature;[47,62–69] see the purple histogram in Figure 5c. A comparison between the two histograms shows that the absolute value of g for our SPEs is about twice that of the free exciton of unstrained WS$_2$ MLs. We also notice that a similar finding was observed for analogous emitters in strained WSe$_2$ MLs.[18–21,23,49,70,71] No correlation is observed between the energy of the emitters and the value of their g-factor, as it can be seen from the inset of Figure 5c.

In the case of WSe$_2$ emitters, it was proposed that this large g value is a consequence of the emitter radiative transition involving an electron in a defect state and a hole in the VB. While the hybridized orbitals $d_{x^2-y^2} \pm id_{xy}$ ($l_z = \pm2h$) constituting the VB are responsible for the intrinsic valley exciton gyromagnetic factor of -4 (the CB d_{z^2} orbitals do no contribute having $l_z = 0$), the defect state adds to the orbital component of g increasing its absolute value.[70] Alternatively, the large gyromagnetic factor reported in the histogram of Figure 5c would be compatible with the value found for dark excitonic species (both neutral and charged) in WS$_2$,[62] WSe$_2$,[72] and WSSe[50] MLs. In our case, the presence of strain and ensuing microscopic disorder could favor dark states state as the origin of the observed emission lines and new experiments are planned to address this point.

3. Conclusions

By creation of hBN/dome heterostructures, we succeeded in preventing the deflation of H$_2$-filled, highly strained TMDC microdomes below the H$_2$ liquefaction temperature ($\approx$32 K). Optical microscopy, μ-Raman, and μ-PL measurements provided evidence of such phenomenon. The strained configuration, kept in place by the hBN layer, is crucial for the appearance of intense narrow lines in the emission spectra of spatially controlled WS$_2$ domes formed in the openings of a lithographically defined mask and brought to 5 K. Second-order autocorrelation measurements confirmed these lines as originating from SPEs. Magneto-μ-PL measurements on the SPEs provided a localized exciton g-factor with a value of about -8. These results confirm the feasibility of our method for the generation of ordered arrays of SPEs in WS$_2$.

Notably, this method does not require any etching procedure on the substrate in order to create stressors and the TMDC ML is also protected from possible sources of contamination since it is naturally lifted up from the bulk crystal by the hydrogen gas pressure. In addition, both our results and several recent reports[27–31] seem to suggest that the formation of TMDC-based SPEs is associated with the presence of sharp strain gradients, such as those present, for example, in proximity of the dome edges. Since the formation of triangular and elliptical domes in predetermined patterns was already achieved,[73] the freedom offered by our nanofabrication method represents an invaluable asset for finding the dome optimal shape and dimensions. Improvements on the emitter intensity and lifetime ($\approx$1–10 ns as determined here by time-resolved μ-PL) can also be explored by deterministically integrating the capped domes with photonic and plasmonic cavities.[28,35,74] The investigation of the coupling of our SPEs with these cavities will be crucially important for unleashing the full potential of TMDC-based SPEs for quantum technologies.

4. Experimental Section

Sample Preparation: The TMDC flakes were exfoliated from bulk crystals (purchased from 2D semiconductors) via the scotch-tape method and were then deposited on SiO$_2$/Si substrates. In the case of the WS$_2$ flakes the sample was covered with a litographically-patterned poly(methyl methacrylate) (PMMA) mask, whose openings allow the formation of ordered arrays of hydrogen-filled domes. The patterned hydrogen irradiation procedure was described in detail in previous works.[13,14,37] The Si substrate on which the flakes were deposited was mounted in a vacuum chamber, connected to an electrical ground and heated to a temperature of $\approx$150 °C. A Kaufman source irradiated the sample with low-energy ($\approx$20 eV) hydrogen ions, which penetrated into the top-most layers of the crystal. In the case of the samples on which the H-opaque mask had been deposited, only the regions that had been left exposed were interested by this phenomenon. The accumulation of molecular hydrogen beneath the first crystal layer led to the formation of spherical domes with footprint depending on the diameter of the mask aperture. In previous works the polymer used for the H-opaque masks was hydrogen silesquioxane (HSQ), which needed to be removed by chemical etching after the hydrogenation treatment.[37] Instead, the PMMA mask used in this work was etched away by the hydrogen ion beam itself, a self-cleaning process, which does not affect the position and sizes of the formed domes. To cap the domes with few-layer hBN, bulk hBN crystals were also exfoliated with the scotch-tape method and few-nm-thick flakes were isolated on PDMS. These flakes were then positioned over the domes via the dry viscoelastic method described in ref. [75]. A wide range of hBN flakes were tested to cap the domes. For relatively thick flakes (>20 nm), it is generally not possible to achieve a good adherence with the domes due to the flake rigidity and consequent capping of air during the deposition process. Good results are generally achieved for thin flakes (<20 nm), provided that the deposition process is performed slowly enough. The domes were observed to remain in shape at low T irrespective of the hBN thickness.

Atomic Force Microscopy Measurements: AFM measurements were performed using a Veeco Digital Instruments Dimension D3100 microscope equipped with a Nanoscope IIIa controller, employing Tapping Mode monolithic silicon probes with a nominal tip curvature radius of 5–10 nm and a force constant of 40 N m^{-1}. All the scans were performed at room temperature and at ambient conditions. All the data were analyzed with the Gwyddion software.

μ-Raman and μ-PL Measurements: μ-Raman spectroscopy on the MoS$_2$ domes was performed by placing the sample on a x–y piezoelectric stage in a closed-cycle He cryostat with variable temperature in order to monitor the evolution of the dome strain, as the hydrogen gas decreases in volume and eventually condenses for temperatures below 32 K.[37] The excitation laser was provided by a single frequency Nd:YVO$_4$

lasers (DPSS series by Lasos) emitting at 532 nm. A 100× objective with NA = 0.75 was employed to excite and collect the light in a backscattering configuration. The laser light was filtered out by a very sharp long-pass Razor edge filter (Semrock). The Raman signal was spectrally dispersed by a 75 cm focal length ACTON SP750 monochromator equipped with a 1200 grooves mm^{-1} grating and detected by a back-illuminated N$_2$-cooled Si CCD camera (100BRX by Princeton Instruments). The μ-Raman spectral resolution was 0.7 cm^{-1}. The ordered arrays of WS$_2$ domes were studied by means of μ-PL spectroscopy, using the same setup just described for the μ-Raman experiments, with the exception of a 20 cm focal length Isoplane 160 monochromator, equipped with 150 and 300 grooves mm^{-1} gratings. A supercontinuum pulsed laser, with 50 ps pulse width and a maximum repetition rate of 77.8 MHz, was used as a source for time-resolved μ-PL measurements, from which the emitter decay times were evaluated. The laser emission was filtered by an acoustic-optic tunable filter tuned at 532 nm. The signal was time analyzed by a Si avalanche photodiode (APD) with nominal 50 ps temporal resolution.

Second-Order Autocorrelation Measurements: The assessment of the emitter single-photon purity was performed with a Hanbury Brown-Twiss setup, which measured the second-order autocorrelation function ($g^{(2)}(\tau)$) of the emitted light. The measurements were performed under continuous-wave excitation via a 532 nm laser. The PL signal coming from the sample was spectrally filtered with a 20 cm focal length Isoplane 160 monochromator, equipped with a 600 grooves mm^{-1} grating. The filtered signal was then divided by a 50/50 beam splitter and collected by two Si avalanche photodiodes with 250 ps temporal resolution. The coincidence counts were calculated by the PicoHarp 300 time-correlated single-photon counting module with a maximum resolution of 4 ps.

μ-PL Measurements Under Magnetic Field: Magneto-μ-PL measurements were performed at low temperature (<10 K) in a superconducting magnet reaching up to 12 T. x–y–z piezoelectric stages were used to excite the sample and collect the signal from the desired point of the sample. A 515-nm-laser and a 100× microscope objective with NA = 0.82 were used. The same objective was used to collect the luminescence. The circular polarization of the luminescence was analyzed using a quarter-wave plate and a Wollaston prism steering the components of opposite linear polarization (and thus of opposite elicity) to different lines of the liquid-nitrogen-cooled Si-CCD (pylon by Princeton Instruments) employed. In this manner, opposite circular polarization components could be acquired simultaneously. A monochromator with 0.75 m focal length and a 600 grooves mm^{-1} grating was used to disperse the PL signal. The field was directed perpendicular to the sample surface (i.e., parallel to the emitted photon wavevector, Faraday configuration).

Supporting Information

Supporting Information is available from the Wiley Online Library or from the author.

Conflict of Interest

The authors declare no conflict of interest.

Data Availability Statement

The data that support the findings of this study are available from the corresponding author upon reasonable request.

Keywords

[1] K. F. Mak, C. Lee, J. Hone, J. Shan, T. F. Heinz, *Phys. Rev. Lett.* **2010**, *105*, 136805.

[2] A. Splendiani, L. Sun, Y. Zhang, T. Li, J. Kim, C.-Y. Chim, G. Galli, F. Wang, *Nano Lett.* **2010**, *10*, 1271.

[3] P. Tonndorf, R. Schmidt, P. Böttger, X. Zhang, J. Börner, A. Liebig, M. Albrecht, C. Kloc, O. Gordan, D. R. T. Zahn, S. M.de Vasconcellos, R. Bratschitsch, *Opt. Express* **2013**, *21*, 4908.

[4] H. Yuan, Z. Liu, G. Xu, B. Zhou, S. Wu, D. Dumcenco, K. Yan, Y. Zhang, S.-K. Mo, P. Dudin, V. Kandyba, M. Yablonskikh, A. Barinov, Z. Shen, S. Zhang, Y. Huang, X. Xu, Z. Hussain, H. Y. Hwang, Y. Cui, Y. Chen, *Nano Lett.* **2016**, *16*, 4738.

[5] L. Zhang, A. Zunger, *Nano Lett.* **2015**, *15*, 949.

[6] A. Pospischil, T. Mueller, *Appl. Sci.* **2016**, *6*, 78.

[7] X. Li, L. Tao, Z. Chen, H. Fang, X. Li, X. Wang, J.-B. Xu, H. Zhu, *Appl. Phys. Rev.* **2017**, *4*, 021306.

[8] T. Mueller, E. Malic, *npj 2D Mater. Appl.* **2018**, *2*, 29.

[9] E. Khestanova, F. Guinea, L. Fumagalli, A. Geim, I. Grigorieva, *Nat. Commun.* **2016**, *7*, 12587.

[10] D. Lloyd, X. Liu, J. W. Christopher, L. Cantley, A. Wadehra, B. L. Kim, B. B. Goldberg, A. K. Swan, J. S. Bunch, *Nano Lett.* **2016**, *16*, 5836.

[11] R. Yang, J. Lee, S. Ghosh, H. Tang, R. M. Sankaran, C. A. Zorman, P. X.-L. Feng, *Nano Lett.* **2017**, *17*, 4568.

[12] D. Lloyd, X. Liu, N. Boddeti, L. Cantley, R. Long, M. L. Dunn, J. S. Bunch, *Nano Lett.* **2017**, *17*, 5329.

[13] C. Di Giorgio, E. Blundo, G. Pettinari, M. Felici, Y. Lu, A. M. Cucolo, A. Polimeni, F. Bobba, *Adv. Mater. Interfaces* **2020**, *7*, 2001024.

[14] E. Blundo, C. Di Giorgio, G. Pettinari, T. Yildirim, M. Felici, Y. Lu, F. Bobba, A. Polimeni, *Adv. Mater. Interfaces* **2020**, *7*, 2000621.

[15] C. Di Giorgio, E. Blundo, G. Pettinari, M. Felici, A. Polimeni, F. Bobba, *ACS Appl. Mater. Interfaces* **2021**, *13*, 48228.

[16] C. Di Giorgio, E. Blundo, G. Pettinari, M. Felici, F. Bobba, A. Polimeni, *Adv. Mater. Interfaces* **2022**, *9*, 2102220.

[17] E. Blundo, E. Cappelluti, M. Felici, G. Pettinari, A. Polimeni, *Appl. Phys. Rev.* **2021**, *8*, 021318.

[18] Y.-M. He, G. Clark, J. R. Schaibley, Y. He, M.-C. Chen, Y.-J. Wei, Q. Z. Xing Ding, W. Yao, X. Xu, C.-Y. Lu, J.-W. Pan, *Nat. Nanotechnol.* **2015**, *10*, 497.

[19] S. Kumar, A. Kaczmarczyk, B. D. Gerardot, *Nano Lett.* **2015**, *15*, 7567.

[20] A. Srivastava, M. Sidler, A. V. Allain, D. S. Lembke, A. Kis, A. Imamoğlu, *Nat. Nanotechnol.* **2015**, *10*, 491.

[21] Y. Koperski, K. Nogajewski, A. Arora, V. Cherkez, P. Mallet, J.-Y. Veuillen, J. Marcus, P. Kossacki, M. Potemski, *Nat. Nanotechnol.* **2015**, *10*, 503.

[22] P. Tonndorf, R. Schmidt, R. Schneider, J. Kern, M. Buscema, G. A. Steele, A. Castellanos-Gomez, H. S.van der Zant, S. M.de Vasconcellos, R. Bratschitsch, *Optica* **2015**, *2*, 347.

[23] C. Chakraborty, L. Kinnischtzke, K. M. Goodfellow, R. Beams, A. N. Vamivakas, *Nat. Nanotechnol.* **2015**, *10*, 507.

[24] C. Palacios-Berraquero, M. Barbone, D. M. Kara, X. Chen, I. Goykhman, D. Yoon, A. K. Ott, J. Beitner, K. Watanabe, T. Taniguchi, A. C. Ferrari, M. Atatüre, *Nat. Commun.* **2016**, *7*, 12978.

[25] A. Branny, G. Wang, S. Kumar, C. Robert, B. Lassagne, X. Marie, B. D. Gerardot, B. Urbaszek, *Appl. Phys. Lett.* **2016**, *108*, 142101.

[26] C. Chakraborty, K. M. Goodfellow, A. N. Vamivakas, *Opt. Mater. Express* **2016**, *6*, 2081.

[27] J. Kern, I. Niehues, P. Tonndorf, R. Schmidt, D. Wigger, R. Schneider, T. Stiehm, S. M.de Vasconcellos, D. E. Reiter, T. Kuhn, R. Bratschitsch, *Adv. Mater.* **2016**, *28*, 7101.

[28] O. Iff, N. Lundt, S. Betzold, L. N. Tripathi, M. Emmerling, S. Tongay, Y. J. Lee, S.-H. Kwon, S. Höfling, C. Schneider, *Opt. Express* **2018**, *26*, 25944.

[29] C. Palacios-Berraquero, D. M. Kara, A. R.-P. Montblanch, M. Barbone, P. Latawiec, D. Yoon, A. K. Ott, M. Loncar, A. C. Ferrari, M. Atatüre, *Nat. Commun.* **2017**, *8*, 15093.

[30] A. Branny, S. Kumar, R. Proux, B. D. Gerardot, *Nat. Commun.* **2017**, *8*, 15053.

[31] T. Cai, J.-H. Kim, Z. Yang, S. Dutta, S. Aghaeimeibodi, E. Waks, *ACS Photonics* **2018**, *5*, 3466.

[32] T. Cai, S. Dutta, S. Aghaeimeibodi, Z. Yang, S. Nah, J. T. Fourkas, E. Waks, *Nano Lett.* **2017**, *17*, 6564.

[33] L. Peng, H. Chan, P. Choo, T. W. Odom, S. K. R. S. Sankaranarayanan, X. Ma, *Nano Lett.* **2020**, *20*, 5866.

[34] Y. Luo, G. D. Shepard, J. V. Ardelean, D. A. Rhodes, B. Kim, K. Barmak, J. C. Hone, S. Strauf, *Nat. Nanotechnol.* **2018**, *13*, 1137.

[35] O. Iff, Q. Buchinger, M. Moczała-Dusanowska, M. Kamp, S. Betzold, M. Davanco, K. Srinivasan, S. Tongay, C. Antón-Solanas, S. Höfling, C. Schneider, *Nano Lett.* **2021**, *21*, 4715.

[36] M. Kianinia, Z.-Q. Xu, M. Toth, I. Aharonovich, *Appl. Phys. Rev.* **2022**, *9*, 011306.

[37] D. Tedeschi, E. Blundo, M. Felici, G. Pettinari, B. Liu, T. Yildrim, E. Petroni, C. Zhang, Y. Zhu, S. Sennato, Y. Lu, A. Polimeni, *Adv. Mater.* **2019**, *31*, 1903795.

[38] E. Blundo, A. Surrente, D. Spirito, G. Pettinari, T. Yildirim, C. A. Chavarin, L. Baldassarre, M. Felici, A. Polimeni, *Nano Lett.* **2022**, *22*, 1525.

[39] E. Blundo, T. Yildirim, G. Pettinari, A. Polimeni, *Phys. Rev. Lett.* **2021**, *127*, 046101.

[40] P. Klemens, *Phys. Rev.* **1966**, *148*, 845.

[41] M. Balkanski, R. Wallis, E. Haro, *Phys. Rev. B* **1983**, *28*, 1928.

[42] C. Postmus, J. Ferraro, S. Mitra, *Phys. Rev.* **1968**, *174*, 983.

[43] L. He, H. Wang, L. Chen, X. Wang, H. Xie, C. Jiang, C. Li, K. Elibol, J. Meyer, K. Watanabe, T. Taniguchi, Z. Wu, W. Wang, Z. Ni, X. Miao, C. Zhang, D. Zhang, H. Wang, X. Xie, *Nat. Commun.* **2019**, *10*, 2851.

[44] G. Wang, A. Chernikov, M. M. Glazov, T. F. Heinz, X. Marie, T. Amand, B. Urbaszek, *Rev. Mod. Phys.* **2018**, *90*, 021001.

[45] D. Vaclavkova, J. Wyzula, K. Nogajewski, A. Bartos, A. Slobodeniuk, C. Faugeras, M. Potemski, M. Molas, *Nanotechnology* **2018**, *29*, 325705.

2202953 (9 of 10)

**ADVANCED
SCIENCE NEWS**

www.advancedsciencenews.com

**ADVANCED
OPTICAL
MATERIALS**

www.advopticalmat.de

[46] E. Blundo, M. Felici, T. Yildirim, G. Pettinari, D. Tedeschi, A. Miri-ametro, B. Liu, W. Ma, Y. Lu, A. Polimeni, *Phys. Rev. Res.* **2020**, *2*, 012024.

[47] E. Blundo, P. E. F. Junior, A. Surrente, G. Pettinari, M. A. Prosnikov, K. Olkowska-Pucko, K. Zollner, T. Woźniak, A. Chaves, T. Kazimierczuk, M. Felici, A. Babiński, M. R. Molas, P. C. M. Christianen, J. Fabian, A. Polimeni, *Phys. Rev. Lett.* **2022**, *129*, 067402.

[48] G. Plechinger, P. Nagler, J. Kraus, N. Paradiso, C. Strunk, C. Schüller, T. Korn, *Phys. Status Solidi RRL* **2015**, *9*, 457.

[49] G. D. Shepard, O. A. Ajayi, X. Li, X.-Y. Zhu, J. Hone, S. Strauf, *2D Mater.* **2017**, *4*, 021019.

[50] K. Olkowska Pucko, E. Blundo, N. Zawadzka, S. Cianci, D. Vaclavkova, P. Kapuściński, D. Jana, G. Pettinari, M. Felici, K. Nogajewski, M. Bar-toš, K. Watanabe, T. Taniguchi, C. Faugeras, M. Potemski, A. Babiński, A. Polimeni, M. R. Molas, *2D Mater.* **2023**, *10*, 015018.

[51] L. Linhart, M. Paur, V. Smejkal, J. Burgdörfer, T. Mueller, F. Libisch, *Phys. Rev. Lett.* **2019**, *123*, 146401.

[52] H. Moon, E. Bersin, C. Chakraborty, A.-Y. Lu, G. Grosso, J. Kong, D. Englund, *ACS Photonics* **2020**, *7*, 1135.

[53] K. Parto, S. I. Azzam, K. Banerjee, G. Moody, *Nat. Commun.* **2021**, *12*, 3585.

[54] L. Chirolli, E. Prada, F. Guinea, R. Roldán, P. San-Jose, *2D Mater.* **2019**, *6*, 025010.

[55] T. P. Darlington, C. Carmesin, M. Florian, E. Yanev, O. Ajayi, J. Arde-lean, D. A. Rhodes, A. Ghiotto, A. Krayev, K. Watanabe, T. Taniguchi, J. W. Kysar, A. N. Pasupathy, J. C. Hone, F. Jahnke, N. J. Borys, P. J. Schuck, *Nat. Nanotechnol.* **2020**, *15*, 854.

[56] C. Carmesin, M. Lorke, M. Florian, D. Erben, A. Schulz, T. O. Wehling, F. Jahnke, *Nano Lett.* **2019**, *19*, 3182.

[57] Y. Ye, X. Dou, K. Ding, D. Jiang, F. Yang, B. Sun, *Phys. Rev. B* **2017**, *95*, 245313.

[58] B. Schuler, K. A. Cochrane, C. Kastl, E. S. Barnard, E. Wong, N. J. Borys, A. M. Schwartzberg, D. F. Ogletree, F. J. G.de Abajo, A. Weber-Bargioni, *Sci. Adv.* **2020**, *6*, eabb5988.

[59] T. Vogl, G. Campbell, B. C. Buchler, Y. Lu, P. K. Lam, *ACS Photonics* **2018**, *5*, 2305.

[60] T. T. Tran, C. Elbadawi, D. Totonjian, C. J. Lobo, G. Grosso, H. Moon, D. R. Englund, M. J. Ford, I. Aharonovich, M. Toth, *ACS Nano* **2016**, *10*, 7331.

[61] Q. Wang, J. Maisch, F. Tang, D. Zhao, S. Yang, R. Joos, S. L. Portalupi, P. Michler, J. H. Smet, *Nano Lett.* **2021**, *21*, 7175.

[62] M. Zinkiewicz, T. Wozniak, T. Kazimierczuk, P. Kapuscinski, K. Oreszczuk, M. Grzeszczyk, M. Bartoš, K. Nogajewski, K. Watanabe, T. Taniguchi, C. Faugeras, P. Kossacki, M. Potemski, A. Babiński, M. R. Molas, *Nano Lett.* **2021**, *21*, 2519.

[63] G. Plechinger, P. Nagler, A. Arora, A. Granados del Águila, M. V. Bal-lottin, T. Frank, P. Steinleitner, M. Gmitra, J. Fabian, P. C. Christianen, R. Bratschitsch, C. Schüller, T. Korn, *Nano Lett.* **2016**, *16*, 7899.

[64] A. V. Stier, K. M. McCreary, B. T. Jonker, J. Kono, S. A. Crooker, *Nat. Commun.* **2016**, *7*, 10643.

[65] R. Schmidt, A. Arora, G. Plechinger, P. Nagler, A. G. Del Águila, M. V. Ballottin, P. C. Christianen, S. M.de Vasconcellos, C. Schüller, T. Korn, R. Bratschitsch, *Phys. Rev. Lett.* **2016**, *117*, 077402.

[66] J. Kuhnert, A. Rahimi-Iman, W. Heimbrodt, *J. Condens. Matter Phys.* **2017**, *29*, 08LT02.

[67] J. Zipfel, J. Holler, A. A. Mitioglu, M. V. Ballottin, P. Nagler, A. V. Stier, T. Taniguchi, K. Watanabe, S. A. Crooker, P. C. Christianen, T. Korn, A. Chernikov, *Phys. Rev. B* **2018**, *98*, 075438.

[68] M. Koperski, M. R. Molas, A. Arora, K. Nogajewski, M. Bartos, J. Wyzula, D. Vaclavkova, P. Kossacki, M. Potemski, *2D Mater.* **2018**, *6*, 015001.

[69] M. Goryca, J. Li, A. V. Stier, T. Taniguchi, K. Watanabe, E. Courtade, S. Shree, C. Robert, B. Urbaszek, X. Marie, S. A. Crooker, *Nat. Commun.* **2019**, *10*, 4172.

[70] J. Dang, S. Sun, X. Xie, Y. Yu, K. Peng, C. Qian, S. Wu, F. Song, J. Yang, S. Xiao, L. Yang, Y. Wang, M. A. Rafiq, C. Wang, X. Xu, *npj 2D Mater. Appl.* **2020**, *4*, 2.

[71] C. S.de Brito, C. R. Rabahi, M. D. Teodoro, D. F. Franco, M. Nalin, I. D. Barcelos, Y. G. Gobato, *Appl. Phys. Lett.* **2022**, *121*, 070601.

[72] M. He, P. Rivera, D. Van Tuan, N. P. Wilson, M. Yang, T. Taniguchi, K. Watanabe, J. Yan, D. G. Mandrus, H. Yu, H. Dery, W. Yao, X. Xu, *Nat. Commun.* **2021**, *11*, 618.

[73] S. Cianci, E. Blundo, M. Felici, A. Polimeni, G. Pettinari, *Opt. Mater.* **2022**, *125*, 112087.

[74] D. Komisar, S. Kumar, Y. Kan, C. Wu, S. I. Bozhevolnyi, *ACS Photonics* **2021**, *8*, 2190.

[75] A. Castellanos-Gomez, M. Buscema, R. Molenaar, V. Singh, L. Janssen, H. S. J.van der Zant, G. A. Steele, *2D Mater.* **2014**, *1*, 011002.

ADVANCED OPTICAL MATERIALS

Supporting Information

Spatially Controlled Single Photon Emitters in hBN-Capped WS_2 Domes

Salvatore Cianci, Elena Blundo, Federico Tuzi, Giorgio Pettinari, Katarzyna Olkowska-Pucko, Eirini Parmenopoulou, Djero B. L. Peeters, Antonio Miriametro, Takashi Taniguchi, Kenji Watanabe, Adam Babinski, Maciej R. Molas, Marco Felici* and Antonio Polimeni*

SUPPORTING INFORMATION for

Spatially controlled single photon emitters in hBN-capped WS$_2$ domes

Salvatore Cianci,[1] Elena Blundo,[1] Federico Tuzi,[1] Giorgio Pettinari,[2] Katarzyna Olkowska-Pucko,[3] Eirini Parmenopoulou,[1] Djero B. L. Peeters,[1,+] Antonio Miriametro,[1] Takashi Taniguchi,[4] Kenji Watanabe,[5] Adam Babinski,[3] Maciej R. Molas,[3] Marco Felici,[1,*] and Antonio Polimeni[1,*]

[1] *Physics Department, Sapienza University of Rome, 00185, Rome, Italy.*
[2] *Institute for Photonics and Nanotechnologies (CNR-IFN), National Research Council, 00133, Rome, Italy*
[3] *Institute of Experimental Physics, Faculty of Physics, University of Warsaw, 02-093 Warsaw, Poland*
[4] *International Center for Materials Nanoarchitectonics, National Institute for Materials Science, 1-1 Namiki, Tsukuba 305-0044, Japan*
[5] *Research Center for Functional Materials, National Institute for Materials Science, 1-1 Namiki, Tsukuba 305-0044, Japan*

[+] Present address: Eindhoven University of Technology, 5600 MB Eindhoven, The Netherlands
[*] Corresponding authors: antonio.polimeni@uniroma1.it, marco.felici@uniroma1.it

Contents

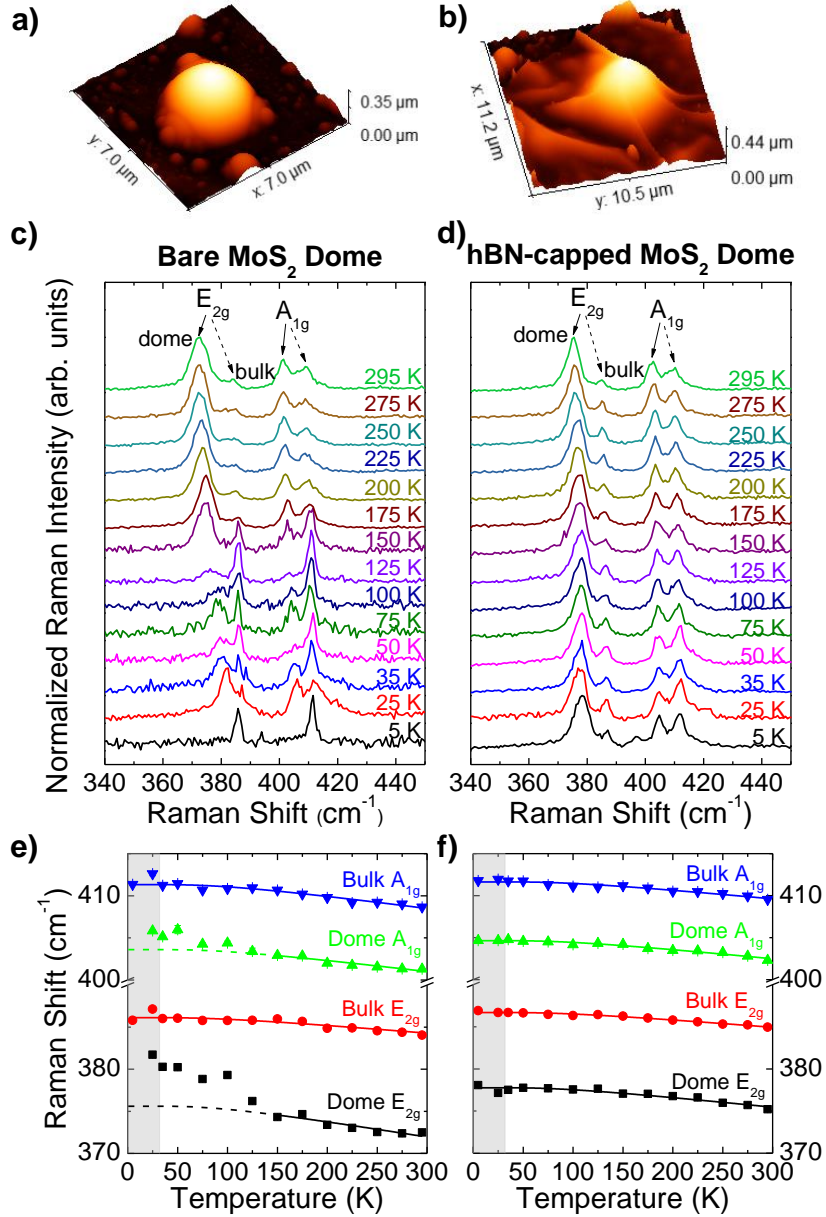## Supporting Figure 1. Raman spectra of a MoS$_2$ dome before and after the capping with hBN.

Figure S1. Temperature-dependent μ-Raman studies of a MoS$_2$ dome before and after capping with few-layer hBN. a)-b) AFM 3D maps of the dome before a) and after b) the capping procedure. c)-d) Stacked μ-Raman spectra for all the temperatures considered of the MoS$_2$ dome before and after hBN capping (laser excitation wavelength equal to 532 nm and laser power equal to 30 μW.). The peaks refer to the E$_{2g}$ (in-plane) and A$_{1g}$ (out-of-plane) modes of oscillation associated to the bulk crystal (dashed arrow) and to the dome membrane (full arrow). e)-f) Evolution with temperature of the peaks of panels c) and d) extracted by performing Lorentzian fits of the μ-Raman spectra of the bare and capped dome. The trends are fitted with $\omega\left(T\right)=\omega_0 + A\left[1 + 2/\left(e^{\frac{\hbar\omega_0}{2k_{\mathrm{B}}T}} - 1\right)\right]$, where only the lower-order three-phonon processes of the anharmonic Klemens model are taken into account via the parameter A.[1,2] The almost

parallel trends of the peaks associated to the bulk crystal and the capped dome of panel f) are in contrast with the erratic behaviour of the bare dome peak of panel e), proving the effect of hBN even for temperatures below the gas-to-liquid transition of H_2 at 32 K (shaded gray area).

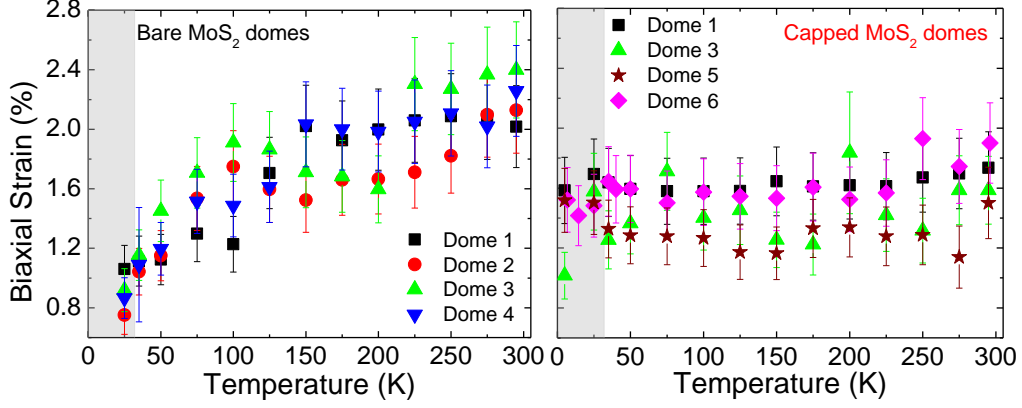## Supporting Figure 2. Statistics on the strain of bare and capped MoS$_2$ domes.

Figure S2. Biaxial strain vs temperature calculated from the Raman shifts of the E$_{2g}$ peak (in-plane mode of oscillation) of several MoS$_2$ domes. The value of strain is calculated using the equation

$$\varepsilon(T) = \frac{1}{2} \cdot \left(\frac{\omega_{E_{2g}}^{ML}(T) - \omega_{E_{2g}}^{dome}(T)}{\omega_{E_{2g}}^{ML}(T)} \right) \frac{1}{\gamma_{E_{2g}}} \tag{2.1}$$

where $\omega_{E_{2g}}^{ML}(T)$ is the Raman shift of the in-plane mode of a strain-free MoS$_2$ ML at temperature T – obtained by adding 1.5 cm^{-1} to the bulk shift – $\gamma_{E_{2g}}$ is the Grüneisen parameter equal to 0.84 ± 0.11[3] (assumed constant at all temperatures[4]) and the total biaxial strain is divided by 2 to obtain the strain exerted on just one direction (*i.e.* the radial or the circumferential one that are equivalent at the top of the dome). The left panel shows the evolution in temperature of the strain of the bare domes, while the right panel that of the strain after the capping with few-layer hBN. At RT the capping procedure leads to a reduction in strain, which is then kept constant at all temperatures. The range of temperatures below the gas-to-liquid transition of H$_2$ is indicated by the shaded gray area.

3

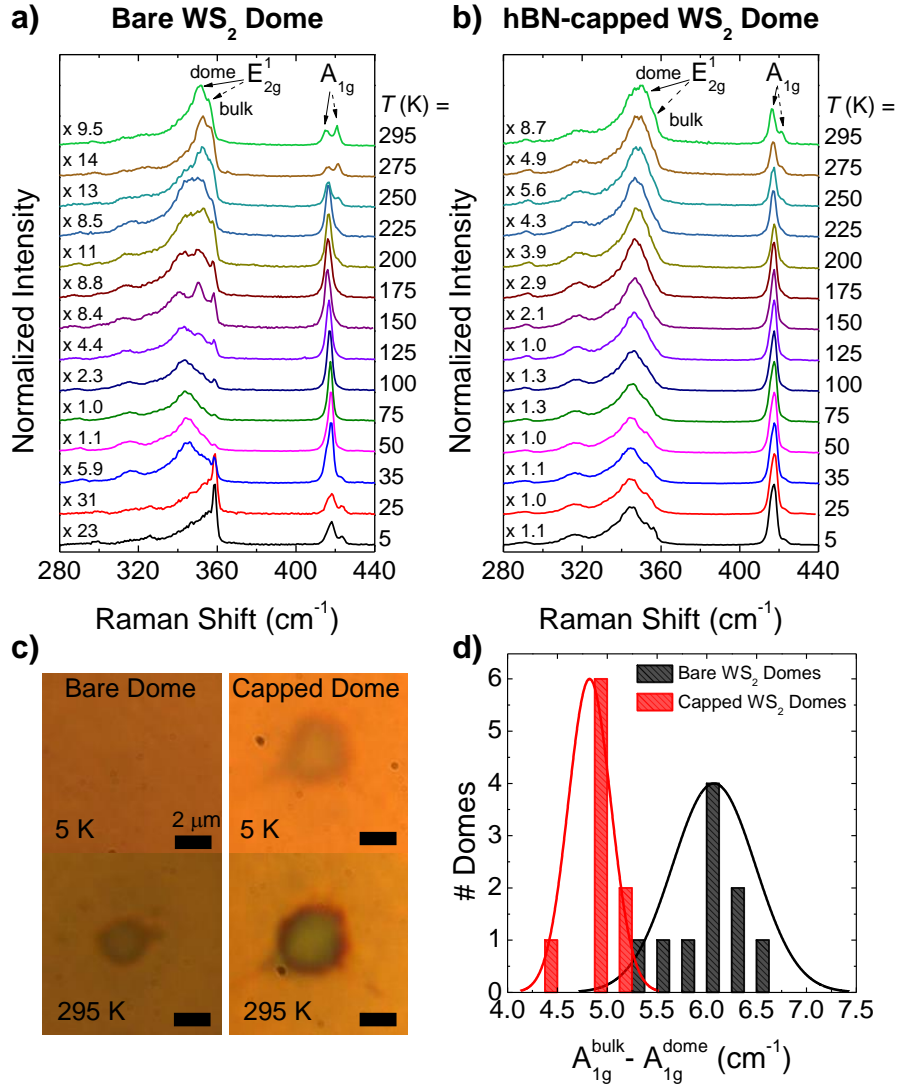## Supporting Figure 3. Raman spectra of bare and hBN-capped WS$_2$ domes.

Figure S3. Raman study of bare and hBN-capped WS$_2$ domes. a)-b) Stacked μ-Raman spectra at different temperatures of a bare a) and hBN-capped b) WS$_2$ dome. The laser excitation wavelength is equal to 532 nm and the laser power is equal to 30 μW. The peaks refer to the E$_{2g}^1$ (in-plane) and A$_{1g}$ (out-of-plane) modes of oscillation associated to the bulk crystal (dashed arrow) and to the dome membrane (full arrow). Next to each spectrum an intensity factor indicates the ratio between the maximum intensity of the corresponding set of spectra and the intensity for that specific temperature. While the bare WS$_2$ dome's spectra show an erratic behaviour both in lineshape and in intensity, the regularity of the capped dome's spectra, on the other hand, reflects the conservative effect of hBN. c) Optical images of the domes of panel a) (left column) and panel b) (right column) at temperatures of 5 K and 295 K. The deflation, at low T, undergone by the bare dome is in contrast with the minimal changes in volume experienced by the hBN-capped dome. Scalebar, 2 μm. d) Histogram collecting the differences in Raman shift, at RT, between the peak associated to the bulk A$_{1g}$ mode of oscillation and the one associated to the dome membrane. The peak values were extracted with Lorentzian fits performed on the spectra of several bare (black bars) and hBN-capped (red bars) WS$_2$ domes. Since strain is responsible for the softening of the Raman mode, the reduction from a mean

value of A_{1g}^{bulk}-$A_{1g}^{bare\ dome}$ = (6.07 ± 0.42) cm^{-1} to a mean value of A_{1g}^{bulk}-$A_{1g}^{capped\ dome}$ = (4.82 ± 0.21) cm^{-1} indicates a reduction of strain experienced by the domes that were capped with few-layer hBN. A more thorough quantitative estimation of strain is prevented both by the clarity of the lines (especially for the E_{2g}^1 mode of oscillation) and by the fact that in the point of maximum strain, *i.e.* the the center of the dome, the Raman signal experiences a significant drop in intensity, so that the peaks that are visible in the previous spectra are most likely related to the emission collected from the lateral portion of the domes, where the strain tensor has a strong spatial dependency.
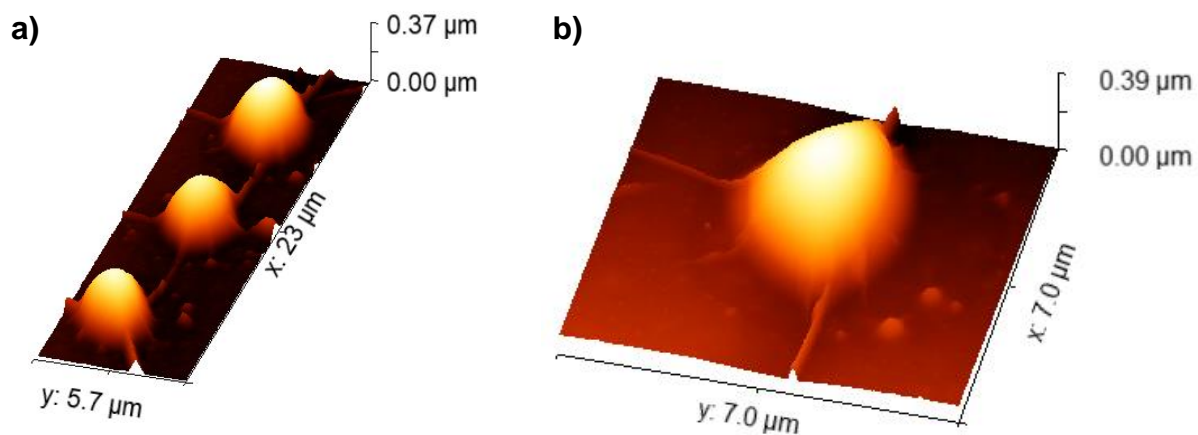
Supporting Figure 4. AFM images of patterned WS$_2$ domes.

Figure S4. a) AFM image of bare WS$_2$ domes formed in the lithographically-defined openings of a PMMA mask. b) Close-up of one of the domes from panel a) showing the nearly total absence of satellite domes at its edge. The lack of smaller secondary domes is a consequence of the application of the PMMA mask and leads to better results during the capping with few-layer hBN. Some wrinkles that can be noticed in the images are likely due to small residuals of PDMS following the capping with hBN applied to a nearby zone.

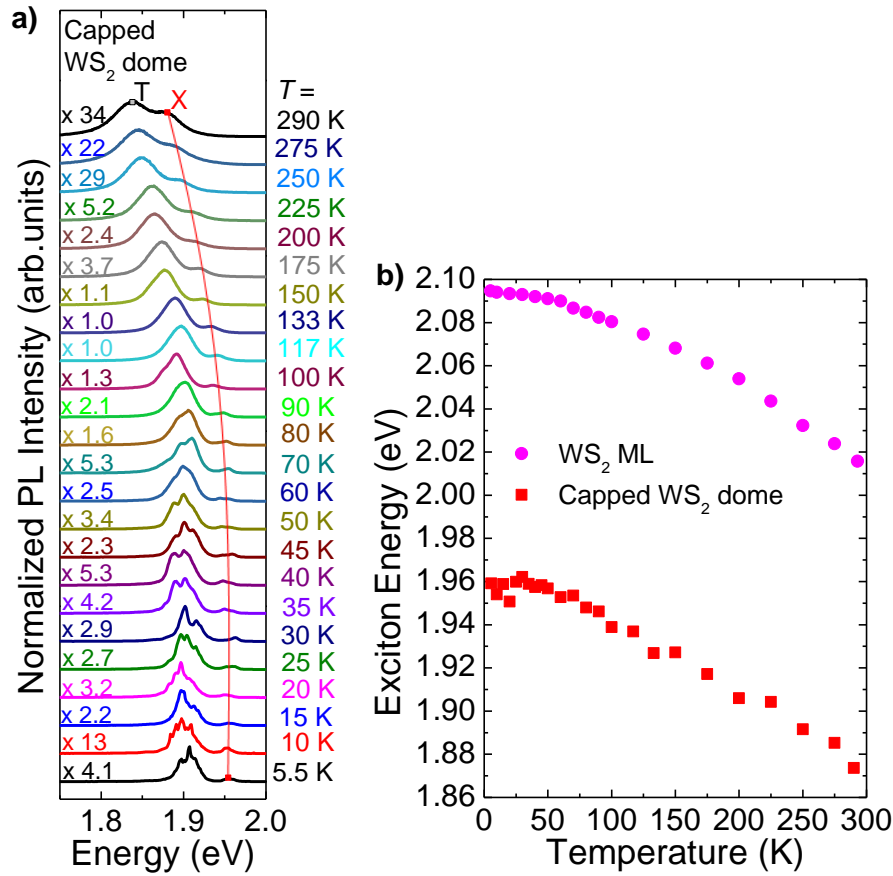## Supporting Figure 5. Evolution in temperature of the PL of a capped WS$_2$ dome.

Figure S5. a) μ-photoluminescence (PL) of a WS$_2$ dome capped with few-layer hBN as a function of temperature. Excitation wavelength equal to 532 nm and laser power equal to 4.4 μW. The exciton peak (X) is highlighted at 290 K and 5.5 K by a red square, with its evolution at intermediate temperatures followed by a red line as a guide for the eye. The predominant energy band at lower energy (labeled T) is likely due to charged exciton recombination.[5,6] The intensity factors next to each spectrum are the ratio between the maximum PL intensity at 117 K and the one of the corresponding spectrum. b) Energy of exciton X vs temperature extracted from the spectra of panel a) via Voigt fits (red squares) compared with the evolution in energy of the exciton peak of an unstrained WS$_2$ ML deposited on SiO$_2$ (magenta circles). Apart from a rigid shift caused by tensile strain, the two trends are almost identical, confirming the preserving effect of hBN on the dome geometry and strained configuration.

Supporting Figure 6. $g-$factor of WS$_2$ quantum emitters.
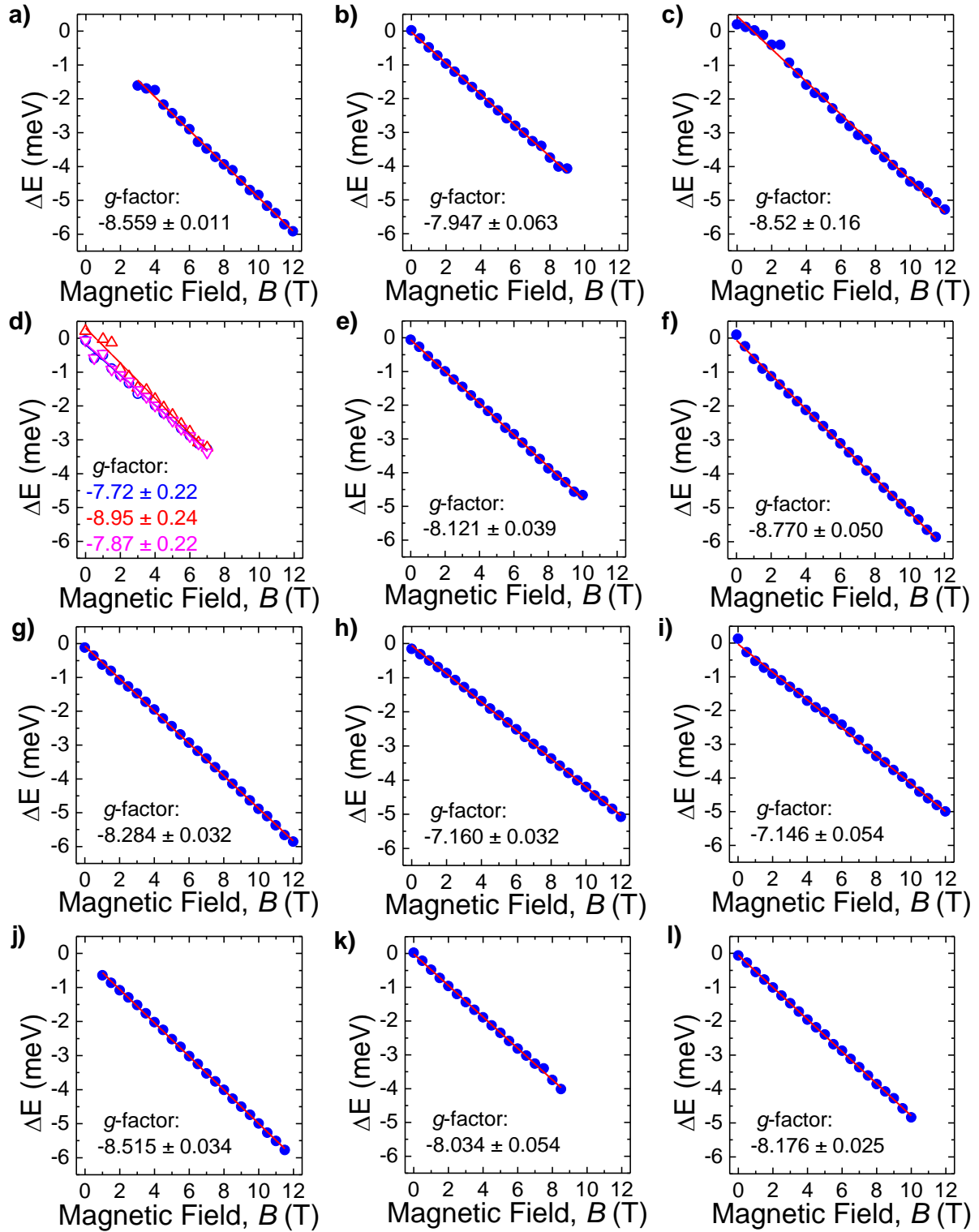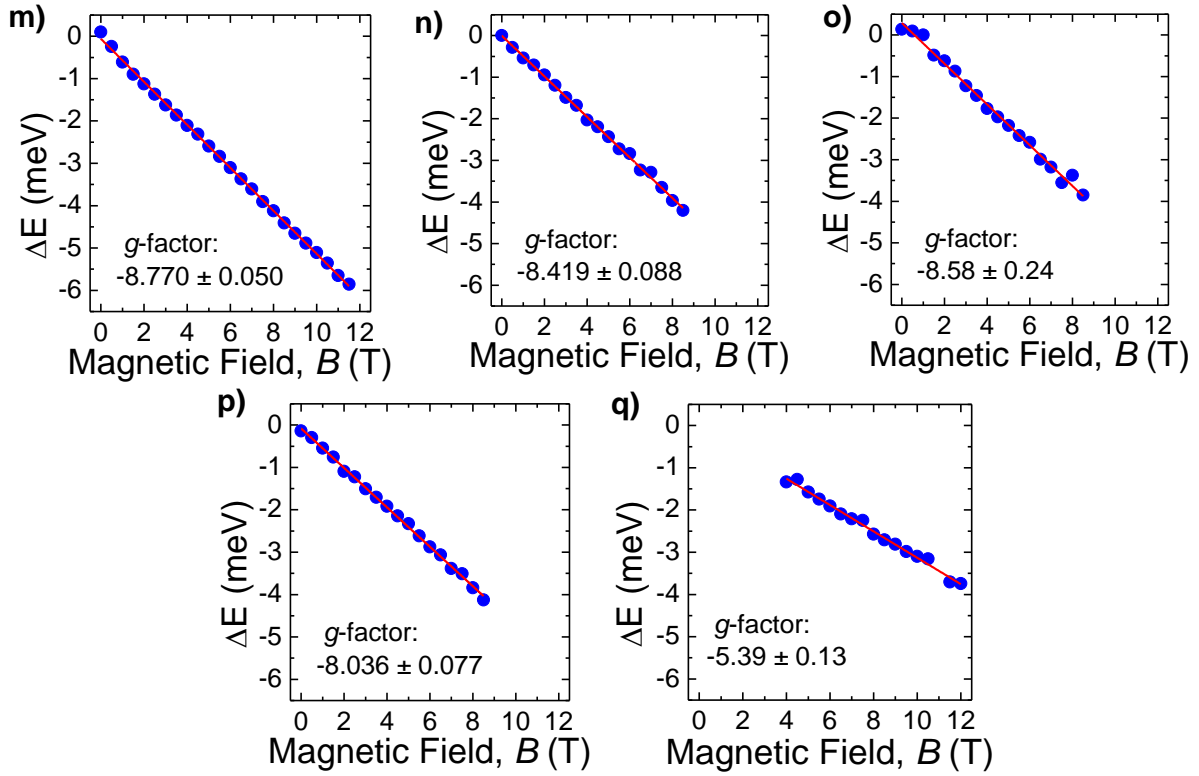

Figure S6.1 *Figure continues in the next page.*

Figure S6.2 *g*-factors of the emitters appearing in the PL spectra of hBN-capped WS$_2$ domes at 10 K. The difference in energy ΔE between the σ^+ and σ^- polarisation (Zeeman splitting) of the emitters is plotted as a function of the applied out-of-plane magnetic field B. The linear fits follow the equation $\Delta E = g\mu_B B$, where μ_B is the Bohr magneton and g is the value of the exciton gyromagnetic factor. Panel d) shows three emitters in the same plot since their emission energies are in a narrow spectral window and were extracted performing a multi-peak Lorentzian fit. A more complete discussion on the distribution of the values of g, extracted from these fits, can be found in the main text. All the points in the plots have an uncertainty of 0.26 meV. Excitation wavelength, 515 nm. Laser powers between 1 μW and 15 μW.

References

[1] P. Klemens, *Phys. Rev.* **1966**, *148,* 845.

[2] M. Balkanski, R. Wallis, E. Haro, *Phys. Rev. B* **1983**, *28,* 1928.

[3] E. Blundo, T. Yildirim, G. Pettinari, A. Polimeni, *Phys. Rev. Lett.* **2021**, *127,* 046101.

[4] C. Postmus, J. Ferraro, S. Mitra, *Phys. Rev.* **1968**, *174,* 983.

[5] G. Plechinger, P. Nagler, J. Kraus, N. Paradiso, C. Strunk, C. Schüller, T. Korn, *Phys. Status Solidi - Rapid Res. Lett.* **2015**, *9,* 457.

[6] D. Vaclavkova, J. Wyzula, K. Nogajewski, M. Bartos, A. Slobodeniuk, C. Faugeras, M. Potemski, M. Molas, *Nanotechnology* **2018**, *29,* 325705.